Solving frequency-domain elastic wave equations via parallel controllability methods

Jet Hoe Tang[1], *Romain Brossier*[1] *and Ludovic Métivier*[1,2]
[1]*Univ. Grenoble Alpes, ISTerre, F-38058 Grenoble, France*
[2]*Univ. Grenoble Alpes, CNRS, LJK, F-38058 Grenoble, France*

SUMMARY

Conventional methods to solve the time-harmonic elastic wave equations usually rely on either direct solvers or iterative solvers. The former are very efficient for treating multiple right hand side problems, as the matrix factorization needs to be done only once for all the right hand sides. However, it suffers from a significant shortcoming associated with high memory consumption and lack of scalability. The latter are matrix-free, and therefore much lighter in memory and scalable. However, dedicated preconditioners are required to converge these methods. The efficiency of existing preconditioners quickly deteriorates as the frequency increases. Another approach to compute time-harmonic solution to elastic wave equations is to consider time-domain solvers. Instead of computing the stationary solution, which convergence is shown to be dependent on the presence of trapped waves and complex wave phenomenon, we develop here a numerical strategy based on a controllability method. The method has been recently analyzed in the frame of acoustic propagation and we extend it here in the frame of linear elasticity. We rely on a spectral element space discretization and a fourth order Runge Kutta time integration. We present the basic properties and formulation of the method, before investigating its scalability and its memory requirement on canonical three-dimensional numerical experiments. The method is shown to be scalable for a problem involving approximately 250 millions degrees of freedom up to more than fifteen hundred computational units.

INTRODUCTION

In the past two decades, 3D Full Waveform Inversion (FWI) has become a key method for velocity modeling building at exploration scales (Virieux and Operto, 2009). While frequency-domain FWI has been the core of the 2D and early 3D implementations (Operto et al., 2006; Brenders and Pratt, 2007; Ben-Hadj-Ali et al., 2008), time-domain formulations have become the standard for the past decade (Warner et al., 2013; Vigh et al., 2014,among many others). However, some researches still focus on the frequency-domain formulation which provides a natural frame for multi-scale FWI (Operto et al., 2015; Operto and Miniussi, 2018).

From standard discretization methods of the frequency-domain wave equation such as finite element (FE) or finite discretization (FD) methods, one typically obtains a large and sparse linear system. The resulting $N \times N$-matrix of, for instance, a three-dimension grid with $N = n^3$ grid points, is sparse and non-Hermitian. This is still a challenge for classical linear system solvers such as direct linear solvers (Operto et al., 2014; Li et al., 2020) or Krylov-based iterative solvers (Plessix, 2009; Li et al., 2014). An LU-based direct linear solver consumes $O(n^4)$ memory to store the dense matrices, so the method quickly reaches its limits as the problem size increases (Li et al., 2020). Although the factorization requires $O(n^6)$ operations, it must be computed only once so the LU direct solver benefits when solving linear systems with multiple right-hand sides from multiple sources. In contrast, the Krylov iterative methods solve the linear systems for each source. But for this, the iterative methods work exclusively with sparse matrices. Moreover, iterative methods terminate when the residual reaches a certain tolerance, where the convergence depends on the system matrix. Modern preconditioners can efficiently accelerate convergence and achieves good parallel scalability (Riyanti et al., 2007; Tsuji et al., 2014). However, convergence deteriorates when tackling higher frequencies (Ernst and Gander, 2012).

Another existing approach relies on the computation of frequency-domain solutions from time-domain solvers (Nihei and Li, 2007; Sirgue et al., 2008), which takes benefit on the reliability and good scaling properties of such solvers. Related to such last methods, the controllability approach has been shown to be very efficient and robust for solving Helmholtz equations (Bristeau et al., 1998; Mönkölä, 2010; Grote and Tang, 2019; Grote et al., 2020). The controllability method (CM) requires repeated solutions of the time-domain wave equation in a short time-window.

In this study, we investigate the CM method for the elastic frequency-domain wave equation and show the good performance of this method in terms of memory requirements, computation time, and parallel scalability. We first consider the time-domain and frequency-domain elastic wave equations and apply a spectral element discretization (Patera, 1984). The CM methods is then detailed and implemented in the frame of the SEM46 full waveform modeling and inversion code (Trinh et al., 2019). Then we present numerical experiments to illustrate the usefulness and efficiency of the CM method, focusing on its parallel performance and memory requirements. We also make a comparison with a standard direct method akin to the LU factorization method used in Li et al. (2020).

TIME-HARMONIC SOLUTION OF ELASTIC WAVE EQUATION WITH A SPECTRAL ELEMENT DISCRETIZATION

The frequency-domain elastic wave equation in $\Omega \subset \mathbb{R}^d$, $d \geq 1$, with a fixed angular frequency $\omega > 0$ is given by

$$-\omega^2 \rho(x)\mathbf{u}(x) - \nabla \cdot \sigma(\mathbf{u}(x)) \;=\; \mathbf{f}(x),\; x \in \Omega, \tag{1}$$

where $\sigma(\mathbf{u}) = \mathbf{C} : \varepsilon(\mathbf{u})$ is the stress tensor with the elastic modulus tensor $\mathbf{C}(\mathbf{x}) = (c_{ijkl}(x))$ and the linearized strain operator $\varepsilon(\mathbf{u}) = \frac{1}{2}(\nabla \mathbf{u}^\intercal + \nabla \mathbf{u})$. Moreover, $\rho(x) \geq \rho_0 > 0$ denotes the density and $\mathbf{f}$ the forcing source.

The transformation of (1) back to the time-domain yields

$$\rho(x)\frac{\partial^2}{\partial^2 t}\mathbf{U}(x,t) - \nabla \cdot \sigma(\mathbf{U}(x,t)) = \mathrm{Re}\{\mathbf{f}(x)\mathrm{e}^{-i\omega t}\}, \tag{2a}$$

$$\mathbf{U}(x,t)\big|_{t=0} = \mathbf{u}_0(x), \tag{2b}$$

$$\dot{\mathbf{U}}(x,t)\big|_{t=0} = \mathbf{v}_0(x), \tag{2c}$$

for $x \in \Omega$ and $t > 0$.

It is clear that the time-harmonic solution $(x,t) \mapsto \mathrm{Re}\{\mathbf{u}(x)\mathrm{e}^{-i\omega t}\}$ solves the time-domain elastic wave equation (2) with the initial conditions $\mathbf{u}_0 = \mathrm{Re}\{\mathbf{u}\}$ and $\mathbf{v}_0 = \omega\,\mathrm{Im}\{\mathbf{u}\}$.

In our implementation, the outgoing waves are absorbed by the first-order absorbing boundary conditions (ABC) on $\partial\Omega$ (Clayton and Engquist, 1977; Engquist and Majda, 1979). To attenuate the reflected waves caused by the non-exact boundary conditions, we additionally combine the ABC with the sponge layer approach (Cerjan et al., 1985; Fletcher et al., 1987).

The variational formulation of (1),

$$-\omega^2 \int_\Omega \rho \mathbf{u}_j \varphi \, dx - \int_\Omega (\nabla \cdot \sigma(\mathbf{u}))_j \varphi \, dx \;=\; \int_\Omega \mathbf{f}_j \varphi \, dx, \tag{3}$$

together with the Galerkin-Ritz ansatz and the (finite) spectral-element method (SEM) via the Gauss-Legendre-Lobatto (GLL) quadrature nodes, yields the linear system

$$\big(-\omega^2 \mathbf{M} + \mathbf{K} - i\omega \mathbf{S}\big)\mathbf{u} = \mathbf{F}. \tag{4}$$

10.1190/segam2021-3583520.1

Here $\mathbf{M}$ denotes the (diagonal) mass matrix, $\mathbf{K}$ the stiffness matrix, $\mathbf{S}$ the absorbing matrix derived from the integration by parts on the stress tensor in (3) and the ABC on the boundary $\partial\Omega$, and $\mathbf{F}$ the discrete forcing source, obtained with the $\mathcal{P}^5$-hexangulation of the computational domain Ω.

The linear system (4), for instance, can be directly solved by the direct solver based on the Gauss elimination and LU factorization method presented in Li et al. (2020). In this study we instead go back to the time-domain and consider the asymptotic limit of (2).

THE LIMITING AMPLITUDE PRINCIPLE AND THE CONTROLLABILITY METHOD

From the limiting amplitude principle in Morawetz (1962) any solution $\mathbf{U}$ to (2) has a time-harmonic asymptotic limit in the sense that

$$\mathbf{U}(x,t) \to \mathrm{Re}\{\mathbf{u}(x)\mathrm{e}^{-i\omega t}\}, \qquad t\to\infty, \tag{5}$$

with the frequency-domain solution $\mathbf{u}(x)$ of (1). Once we found

$$\mathbf{U}(x,t) = \mathrm{Re}\{\mathbf{u}(x)\mathrm{e}^{-i\omega t}\}, \tag{6}$$

we can immediately write

$$\mathbf{u}(x) = \left(1+\frac{i}{\omega}\frac{\partial}{\partial t}\right)\mathbf{U}(x,t)\Big|_{t=mT} \tag{7}$$

with the time period $T=\frac{2\pi}{\omega}$ for $m\geq 0$. In other words, letting the wave equation propagates in a long-term yields the solution of (1) (Nihei and Li, 2007). However, in the presence of physical boundary conditions on the free surface the wave may be trapped or contain resonance such that the convergence may deteriorate and be slow – see Grote and Tang (2019); Grote et al. (2020).

Therefore, we instead adopt the controllability method (CM) based on Bristeau et al. (1998); Mönkölä (2010) to find a T-time periodic solution to (2),

$$\mathbf{U}(x,T) = \mathbf{u}_0(x), \quad \dot{\mathbf{U}}(x,T) = \mathbf{v}_0(x), \qquad x\in\Omega, \tag{8}$$

where the initial pair $(\mathbf{u}_0,\mathbf{v}_0)$ is unknown. In Grote and Tang (2019); Grote et al. (2020,Theorem 1) any (acoustic) T-time periodic solution is given by series of eigenmodes. That results can be directly applied in an analogous way to elastic wave equations and we consequently obtain

$$\mathbf{U}(x,t) = \mathrm{Re}\{\mathbf{u}(x)\mathrm{e}^{-i\omega t}\} + \gamma_0(x) + \sum_{\ell>1}\mathrm{Re}\{\gamma_\ell(x)\mathrm{e}^{-i\omega\ell t}\}, \tag{9}$$

where the eigenmode γ_ℓ solves (1) with $\omega\ell$ instead of ω and $\mathbf{f}=0$ for $\ell=0$ and $\ell>1$. In order to extract the desired mode (6) to get (7), we propose the filtering procedure

$$\mathbf{U}(x,t) \mapsto \hat{\mathbf{u}}(x) := \frac{2}{T}\int_0^T \mathbf{U}(x,t)\mathrm{e}^{i\omega t}\,dt. \tag{10}$$

Then Proposition 1 in Grote et al. (2020) yields

$$\hat{\mathbf{u}}(x) = \mathbf{u}(x). \tag{11}$$

To find an initial pair $(\mathbf{u}_0,\mathbf{v}_0)$ such that the solution $\mathbf{U}$ of (2) is T-time periodic, we formulate the problem as a PDE-constrained optimization problem,

$$\min_{\mathbf{u}_0,\mathbf{v}_0} J(\mathbf{u}_0,\mathbf{v}_0) \tag{12}$$

with the cost functional J given by

$$J(\mathbf{u}_0,\mathbf{v}_0) = \frac{1}{2}\big\|\mathbf{U}(\cdot,T)-\mathbf{u}_0\|_{\mathbf{C}}^2 + \frac{1}{2}\|\dot{\mathbf{U}}(\cdot,T)-\mathbf{v}_0\|_\rho^2 \tag{13}$$

and

$$\|\mathbf{v}\|_{\mathbf{C}}^2 = \int_\Omega (\mathbf{C}:\varepsilon(\mathbf{v})):\varepsilon(\mathbf{v})\,dx, \qquad \|\mathbf{v}\|_\rho^2 = \int_\Omega \rho|\mathbf{v}|^2\,dx. \tag{14}$$

The state variable $\mathbf{U}=\mathbf{U}[\mathbf{u}_0,\mathbf{v}_0]$ solves (2) and depends on the control variable $(\mathbf{u}_0,\mathbf{v}_0)$. Under suitable assumptions on $\mathbf{C}$, like symmetry and positive definiteness, the cost function J is quadratic and convex so that the conjugate gradient (CG) method is a natural candidate of choice for solving (12).

The gradient-based CG method combined with the adjoint-state method requires at each CG iteration the solution of the forward $\mathbf{U}$ and backward $\mathbf{V}$ elastic wave equation. Unlike the full waveform inversion, we only consider the initial and final states of $\mathbf{U}$ and $\mathbf{V}$, so we do not need to store the entire history of $\mathbf{U}$ for the backward equation.

Since the gradient $(J'_u,J'_v)=J'$ of J in u-direction only lies on its dual space, at each CG iteration we have to find a Riesz representative $\mathbf{g}_u$ of J'_u in a more regular space, leading to another linear system

$$\nabla\cdot\sigma(\mathbf{g}_u) = J'_u \qquad \text{in } \Omega. \tag{15}$$

The system matrix here is real-valued, symmetric, and positive definite so that we again apply the (inner) CG method for solving (15).

NUMERICAL METHODS

The main computation in the controllability approach is in solving the elastic forward and backward wave equation (2) and the inner CG loop (15). First, to solve the time-integration of (2), we consider its variational formulation for a fixed $t>0$ given by

$$\int_\Omega \rho\ddot{\mathbf{U}}_j(t)\varphi\,dx - \int_\Omega \nabla\cdot\sigma(\mathbf{U}(t))_j\varphi\,dx = \int_\Omega \mathrm{Re}\{\mathbf{f}_j\mathrm{e}^{-i\omega t}\}\varphi\,dx. \tag{16}$$

Adopting the SEM to (16) we obtain the semi-discrete system of ordinary differential equations,

$$\frac{\partial^2}{\partial^2 t}\mathbf{M}\mathbf{U}(t) + \mathbf{K}\mathbf{U}(t) + \frac{\partial}{\partial t}\mathbf{S}\mathbf{U}(t) = \mathrm{Re}\{\mathbf{F}\mathrm{e}^{-i\omega t}\}, \tag{17}$$

which is solved by the explicit fourth-order Runge-Kutta (RK4) method. The bottleneck associated with the CFL restriction of this explicit method, is compensated by the fact that we only solve (17) in one (short) period $[0,T]$. Moreover the total number of time steps n_T decreases while the frequency increases.

The RK4 operates in the first order formulation of (17), which has the advantage of already having the approximation of $\mathbf{U}(t_m)$ and $\dot{\mathbf{U}}(t_m)$ at each time $t_m=m\Delta t$ for the time step $\Delta t>0$ and $m\geq 0$. The first-order derivative $\dot{\mathbf{U}}(t)$ is used in the Hermite interpolation for the numerical integration of (10) over $[t_m,t_{m+1}]$. The filtering procedure (10) is done by summing up all integrations over the subinterval on the fly so that it is not necessary to store the entire solution of $\mathbf{U}(t_m)$, $m=0,\ldots,n_T$. Moreover, since the mass matrix $\mathbf{M}$ in the SEM approach is diagonal, the RK4 method is fully explicit, fully benefit from the optimized matrix-free implementation of SEM46, and is thus inherently parallel. Second, the formulation of both the outer and inner CG loops requires only basic matrix-vector products, implying the stiffness matrix $\mathbf{K}$, and vector-vector multiplications.

NUMERICAL EXPERIMENTS

Pointsource problem

We first compare the CMCG method with the direct linear solver from Li et al. (2020) for solving (1) with an external point forcing source term located in the center of $\Omega=(0,2.5km)^3$. Second, to show the efficiency of the CMCG method by solving a larger problem, we increase the frequency from $20Hz$ to $40Hz$ and $80Hz$, and respectively the $\mathcal{P}^5$-SE mesh from $28\times28\times28$ to $48\times48\times48$ and $88\times88\times88$. To investigate the scalability in elapsed timing of the CMCG method with the MPI implementation, we repeatedly apply the CMCG method to (1) for a fixed setting and increase the number of cores.

n_{SP}	n_{DOFs}/λ	$V_P[\frac{m}{s}]$	$V_S[\frac{m}{s}]$	$\rho[\frac{g}{m^3}]$	f [Hz]
4	5	5000	2500	1	20

Table 1: Parameter settings: velocities V_p and V_s, density ρ, frequency f, number of elements in the sponge layer n_{SP} in each dimension, and number of points per wavelength λ.

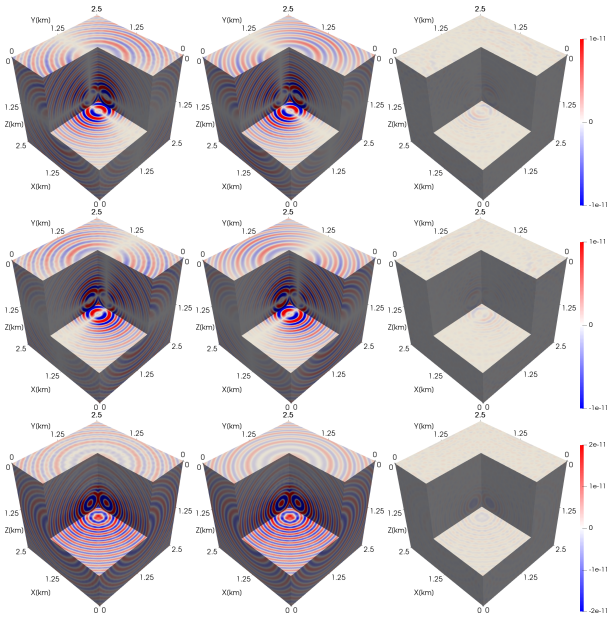

Figure 1: Wavefields u_x (1st row), u_y (2nd row), and u_z (3rd row) of the point source problem at 20$[Hz]$, obtained with the CMCG method (1st column) and the direct solver (2nd column). The numerical differences between both methods are shown in the 3rd column.

The RK4 method is applied to simulations for solving the time integration of (2) with a total number of time steps $n_T = 48$. The CG tolerance of the inner and outer CG loops for the stopping criterion is set to 10^{-4}.

Comparison between the CMCG method and the MUMPS solver
Here we consider both the CMCG method and the direct linear solver based on the LU factorization method. The parameters are listed in Table 1. The computational domain totally consists of $28 \times 28 \times 28$ $\mathcal{P}^5$-SE with 4 sponge elements in each direction. In Table 2, we present the comparison between the numerical solutions, obtained with the CMCG method and the direct solver using the MUMPS package (Li et al., 2020). It can be seen that the CMCG method requires less computation time and particularly less memory. However, the CMCG solution has less accuracy than the direct solution which may be caused by computational error in time and/or less efficient absorbing boundary conditions.

Figure 1 illustrates the CMCG solution (1st column), the MUMPS solution (2nd column), and the difference between both methods (3rd column).

Memory consumption and elapsed time in parallel implementation

In Li et al. (2020), it is very challenging to adopt the direct linear solver and MUMPS for solving (1) with higher frequencies such as 40 and 80 Hz. Especially, the memory requirement quickly reaches limits of conventional computational resources in national HPC centers. In contrast, the CMCG method only requires modest amount of memory, which is shown in Table 3.

	#Cores	**Elapsed Timing**	**Max alloc. Mem.**	**rel. L^2 error** u_x	u_y	u_z
MUMPS	256	855s	1423 GB	4.6%	4.6%	8.7%
CMCG	64	633s	1.6 GB	8%	8%	11.4%

Table 2: Comparison between the CMCG method and MUMPS direct solver with respect to the memory consumption, computational time, and numerical error.

f	n_{DOFs}	**#{Cores}**	**Estim. memory**	**CG iterations**	**Elapsed timing**
20[Hz]	8.4M	8	1.5 GB	175	4163s
		16	1.6 GB	175	2419s
		24	1.6 GB	175	1646s
		32	1.6 GB	175	1355s
		48	1.6 GB	175	919s
		64	1.6 GB	175	619s
40[Hz]	42M	128	7.9 GB	275	2785s
		192	8.0 GB	275	1858s
		256	8.0 GB	275	1384s
		384	8.1 GB	275	880s
		512	8.2 GB	275	602s
80[Hz]	257.3M	768	48.6 GB	483	5152s
		1024	48.0 GB	483	3878s
		1536	49.5 GB	483	2851s

Table 3: Point source: total computational time and estimated allocated memory of the CMCG method by increasing the number of cores for a fixed frequency f, total number of CG iterations in the outer loop and number of degrees of freedoms.

This is expected as the CMCG method only consists of matrix-vector multiplications and is inherently parallel. Figure 2 also confirm the good scalability of this method in the MPI implementation, up to more than fifteen hundred cores. The stopping criterion of the outer CG loop in the CMCG method refers to the relative CG residual is shown in Figure 3 (left), which is nearly independent of the number of cores. The method stops as soon the tolerance 10^{-4} is reached. In Figure 3 (right), we observe that almost 37% of the computation is spent in the inner CG loops and 62% in solving (2).

Figure 4 illustrates the numerical solutions of the point source problem at 80 Hz, obtained with the CMCG method, as well as the analytical solutions, and the analytical errors.

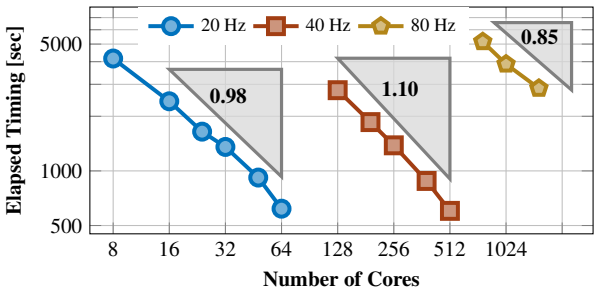

Figure 2: Point source at $f = 20$, 40, and 80 Hz: total elapsed timing spent in the CMCG method by increasing the total number of cores.

CMCG method for elastic problems in heterogeneous medium
Here we apply the CMCG method together with the $\mathcal{P}^5$-SEM and the RK4 method to solve the Marmousi problem with a point source at 40 Hz and $(1.95km, 0.1km, 0.5km)$. We have instead a free surface on

10.1190/segam2021-3583520.1

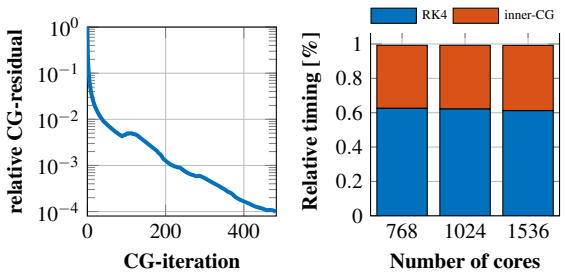

Figure 3: Pointsource 80Hz: (left) convergence of the outer CG loop; (right) elapsed timing in the inner CG loops and in the wave propagation solver (RK4).

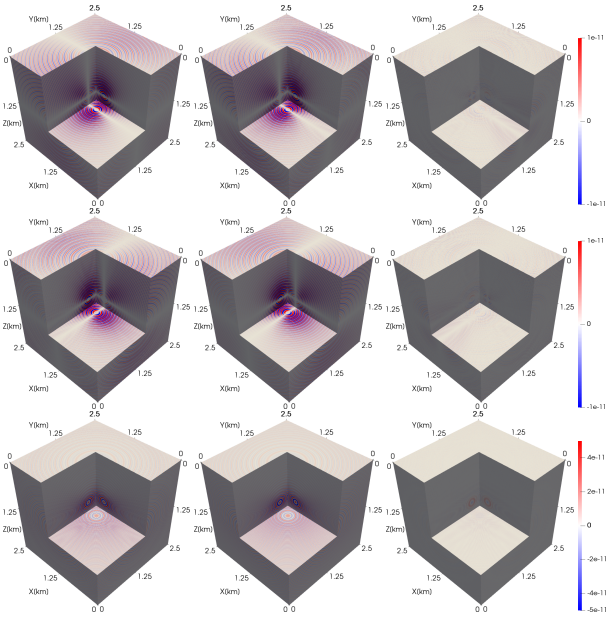

Figure 4: wavefields u_x (1st row), u_y (2nd row), and u_z (3rd row) of the point source problem of 80Hz, obtained with the CMCG method (1st column), the analytical solutions (2nd column), and the analytical errors (3rd column).

the top $\{z = 0\}$ of $\Omega = (0, 3.9km) \times (0, 14km) \times (0, 10km)$. Table 4 illustrates the elapsed time solving (1) with 512 and 1024 cores. From 512 to 1024 cores, we observe a doubling of speed, indicating linear scalability. In Figure 5 we show a cross section from the numerical solution to Marmousi problem, obtained with the CMCG method.

CONCLUSION AND PERSPECTIVES

The controllability method (CM), combined with the conjugate gradient (CG) method, is proposed to find a time-periodic solution of the elastic wave equation, which immediately yields the frequency-domain elastic solution. Although the time-periodic solution may contain additional numerical errors involved by the mass-lumping and numerical errors in the time integration and deficiency from inexact periodicity, the results is still comparable accurate to the solution obtained with a direct linear solver.

The main analysis proves that the filtering procedure extends the original CMCG method in Mönkölä (2010) from elastic sound-soft scattering problems to more general elastic problems.

f	n_{DOFs}	#{Cores}	Estim. memory	CG iterations	Elapsed timing
40 [Hz]	178.7M	512	34 GB	401	4502.0s
		1024	34 GB	401	2185.3s

Table 4: Marmousi 40Hz: total computational time of the CMCG method with 512 and 1024 cores, total number of CG iterations in the outer loop, as well as the number of degrees of freedoms.

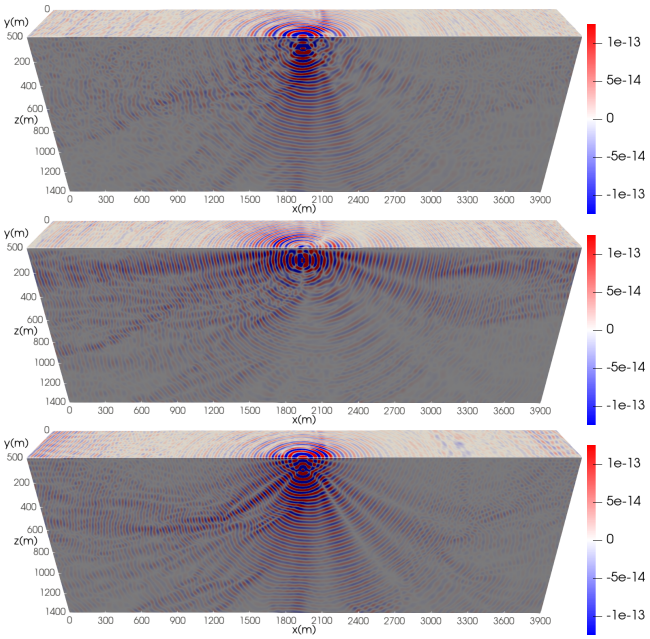

Figure 5: wavefields u_x (1st row), u_y (2nd row), and u_z (3rd row) of the Marmousi problem at 40Hz, obtained with the CMCG method.

Numerical experiments illustrate the usefulness, efficiency, and good parallel scalability of the CMCG method. We observe that most of the computational efforts are spent either in the forward and backward wave propagation solver or in the inner CG loop, which are both inherently parallel. To speed up the inner CG loop, we consider in the future include preconditioners such as a Jacobi preconditioner.

An appropriate initial guess of the frequency-domain solution is also significant to speed up the convergence of the outer loop so that an initial run-up process as proposed in Bristeau et al. (1998); Grote et al. (2020) could be considered. A scattered field formulation could also be used to take benefit from an already known solution in a medium close from the one investigated (Taflove and Hagness, 2005; Pageot et al., 2013). This known solution could be an analytical solution in a simple medium, a solution based on travel-times computed with an eikonal solver, or a full waveform time-harmonic solution computed in a previous medium in the frame of full waveform inversion. This will be the matter of future investigations.

ACKNOWLEDGMENTS

This study has been partially funded by the SEISCOPE consortium (`https://seiscope2.osug.fr`), sponsored by AKERBP, CGG, CHEVRON, EQUINOR, EXXON-MOBIL, JGI, SHELL, SINOPEC, SISPROBE and TOTAL. This study was granted access to the HPC resources of CIMENT infrastructure (`https://ciment.ujf-grenoble.fr`) and CINES/ IDRIS/ TGCC under the allocation 046091 made by GENCI.

REFERENCES

Ben-Hadj-Ali, H., S. Operto, and J. Virieux, 2008, Velocity model building by 3D frequency-domain, full- waveform inversion of wide-aperture seismic data: Geophysics, **73**, no. 5, WE101–WE117, doi: https://doi.org/10.1190/1.2957948.

Brenders, A. J., and R. G. Pratt, 2007, Efficient waveform tomography for lithospheric imaging: Implications for realistic 2D acquisition geometries and low frequency data: Geophysical Journal International, **168**, 152–170, doi: https://doi.org/10.1111/j.1365-246X.2006.03096.x.

Bristeau, M. O., R. Glowinski, and J. Périaux, 1998, Controllability methods for the computation of time-periodic solutions; application to scattering: Journal of Computational Physics, **147**, 265–292, doi: https://doi.org/10.1006/jcph.1998.6044.

Cerjan, C., D. Kosloff, R. Kosloff, and M. Reshef, 1985, A nonreflecting boundary condition for discrete acoustic and elastic wave equations: Geophysics, **50**, 705–708, doi: https://doi.org/10.1190/1.1441945.

Clayton, R., and B. Engquist, 1977, Absorbing boundary conditions for acoustic and elastic wave equations: Bulletin of the Seismological Society of America, **67**, 1529–1540.

Engquist, B., and A. Majda, 1979, Radiation boundary conditions for acoustic and elastic wave calculations: Communications on Pure and Applied Mathematics, **32**, 313–357, doi: https://doi.org/10.1002/cpa.3160320303.

Ernst, O. G., and M. J. Gander, 2012, Why it is difficult to solve helmholtz problems with classical iterative methods, in I. G. Graham, T. Y. Hou, O. Lakkis, and R. Scheichl, eds., Numerical Analysis of Multiscale Problems, volume **83** of Lecture Notes in Computational Science and Engineering: Springer, 325–363.

Fletcher, W. R., J. George, R. Kubichek, S. Smithson, and J. Sochacki, 1987, Absorbing boundary conditions and surface waves: Geophysics, **52**, 60–71, doi: https://doi.org/10.1190/1.1442241.

Grote, M. J., F. Nataf, J. H. Tang, and P.-H. Tournier, 2020, Parallel controllability methods for the Helmholtz equation: Computer Methods in Applied Mechanics and Engineering, **362**, 112846, doi: https://doi.org/10.1016/j.cma.2020.112846.

Grote, M. J., and J. H. Tang, 2019, On controllability methods for the Helmholtz equation: Journal of Computational and Applied Mathematics, **358**, 306–326, doi: https://doi.org/10.1016/j.cam.2019.03.016.

Li, Y., R. Brossier, and L. Métivier, 2020, 3D frequency-domain elastic wave modeling with spectral-element method using a massively parallel direct solver: Geophysics, **85**, no. 2, T71–T88, doi: https://doi.org/10.1190/geo2019-0172.1.

Li, Y., L. Métivier, R. Brossier, B. Han, and J. Virieux, 2014, 2D and 3D frequency-domain elastic wave modeling in complex media with a parallel iterative solver: Geophysics, **80**, no. 3, T101–T118, doi: https://doi.org/10.1190/geo2014-0480.1.

Mönkölä, S., 2010, Time-harmonic solution for acousto-elastic interaction with controllability and spectral elements: Journal of Computational and Applied Mathematics, **234**, 1904–1911, doi: https://doi.org/10.1016/j.cam.2009.08.040.

Morawetz, C., 1962, The limiting amplitude principle: Communications on Pure and Applied Mathematics, **15**, 349–361, doi: https://doi.org/10.1002/cpa.3160150303.

Nihei, K. T., and X. Li, 2007, Frequency response modelling of seismic waves using finite difference time domain with phase sensitive detection (TD-PSD): Geophysical Journal International, **169**, 1069–1078, doi: https://doi.org/10.1111/j.1365-246X.2006.03262.x.

Operto, S., R. Brossier, L. Combe, L. Métivier, A. Ribodetti, and J. Virieux, 2014, Computationally-efficient three- dimensional visco-acoustic finite-difference frequency-domain seismic modeling in vertical transversely isotropic media with sparse direct solver: Geophysics, **79**, no. 5, T257–T275, doi: https://doi.org/10.1190/geo2013-0478.1.

Operto, S., and A. Miniussi, On the role of density and attenuation in three-dimensional multiparameter viscoacoustic VTI frequency-domain FWI: An OBC case study from the North Sea: Geophysical Journal International, **213**, 2037–2059, doi: https://doi.org/10.1093/gji/ggy103.

Operto, S., A. Miniussi, R. Brossier, L. Combe, L. Métivier, V. Monteiller, A. Ribodetti, and J. Virieux, 2015, Efficient 3- D frequency-domain mono-parameter full-waveform inversion of ocean-bottom cable data: application to Valhall in the visco-acoustic vertical transverse isotropic approximation: Geophysical Journal International, **202**, 1362–1391, doi: https://doi.org/10.1093/gji/ggv226.

Operto, S., J. Virieux, J. X. Dessa, and G. Pascal, 2006, Crustal imaging from multifold ocean bottom seismometers data by frequency-domain full-waveform tomography: Application to the eastern Nankai trough: Journal of Geophysical Research, **111**, B09306, doi: https://doi.org/10.1029/2005JB003835.

Pageot, D., S. Operto, M. Vallée, R. Brossier, and J. Virieux, 2013, A parametric analysis of two-dimensional elastic full waveform inversion of teleseismic data for lithospheric imaging: Geophysical Journal International, **193**, 1479–1505, doi: https://doi.org/10.1093/gji/ggs132.

Patera, A. T., 1984, A spectral element method for fluid dynamics: laminar flow in a channel expansion: Journal of Computational Physics, **54**, 468–488, doi: https://doi.org/10.1016/0021-9991(84)90128-1.

Plessix, R. E., 2009, Three-dimensional frequency-domain full-waveform inversion with an iterative solver: Geophysics, **74**, no. 6, WCC149–WCC157, doi: https://doi.org/10.1190/1.3211198.

Riyanti, C. D., A. Kononov, Y. A. Erlangga, C. Vuik, C. Oosterlee, R. E. Plessix, and W. A. Mulder, 2007, A parallel multigrid-based preconditioner for the 3D heterogeneous high-frequency Helmholtz equation: Journal of Computational Physics, **224**, 431–448, doi: https://doi.org/10.1016/j.jcp.2007.03.033.

Sirgue, L., J. T. Etgen, and U. Albertin, 2008, 3D frequency domain waveform inversion using time domain finite difference methods: 70th Annual International Conference and Exhibition, EAGE, Extended Abstracts, F022.

Taflove, A. and S. C. Hagness, 2005, Computational Electrodynamics: The Finite-difference Time-domain Method: Artech House, 3rd edition.

Trinh, P. T., R. Brossier, L. Métivier, L. Tavard, and J. Virieux, 2019, Efficient 3D time-domain elastic and viscoelastic full waveform inversion using a spectral-element method on flexible Cartesian-based mesh: Geophysics, **84**, no. 1, R75–R97, doi: https://doi.org/10.1190/geo2018-0059.1.

Tsuji, P., J. Poulson, B. Engquist, and L. Ying, 2014, Sweeping preconditioners for elastic wave propagation with spectral element methods: ESAIM: Mathematical Modelling and Numerical Analysis, **48**, 433–447, doi: https://doi.org/10.1051/m2an/2013114.

Vigh, D., K. Jiao, D. Watts, and D. Sun, 2014, Elastic full-waveform inversion application using multicomponent measurements of seismic data collection: Geophysics, **79**, no. 2, R63–R77, doi: https://doi.org/10.1190/geo2013-0055.1.

Virieux, J., and S. Operto, 2009, An overview of full waveform inversion in exploration geophysics: Geophysics, **74**, no. 6, WCC1–WCC26, doi: https://doi.org/10.1190/1.3238367.

Warner, M., A. Ratcliffe, T. Nangoo, J. Morgan, A. Umpleby, N. Shah, V. Vinje, I. Stekl, L. Guasch, C. Win, G. Conroy, and A. Bertrand, 2013, Anisotropic 3D full-waveform inversion: Geophysics, **78**, no. 2, R59–R80, doi: https://doi.org/10.1190/geo2012-0338.1.